Alternans and spiral breakup in a human ventricular tissue model

March 6, 2006

Ten Tusscher K. H. W. J.[1] Panfilov A. V.[1]

Running head: Alternans in human ventricular tissue

Contact information: Address for reprint requests and other correspondence: K.H.W.J. ten Tusscher, Utrecht University, Department of Theoretical Biology, Padualaan 8,3584 CH Utrecht, The Netherlands, telephone:+0031(0)30-2533695 fax:+0031(0)30-2513655 e-mail: khwjtuss@hotmail.com

[1]Utrecht University, Department of Theoretical Biology, Padualaan 8, 3584 CH Utrecht, The Netherlands

Abstract

Ventricular fibrillation is one of the main causes of death in the western world. According to one hypothesis, the chaotic excitation dynamics during VF are the result of dynamical instabilities in action potential duration which occurrence requires that the slope of the APD restitution curve exceeds one. Other factors such as electrotonic coupling and cardiac memory also determine whether these instabilities can develop. In this manuscript we study the conditions for alternans and spiral breakup in human cardiac tissue. Therefore, we develop a new version of our human ventricular cell model, which is based on recent experimental measurements of human APD restitution and includes a more extensive description of intracellular calcium dynamics.

We apply this model to study the conditions for electrical instability in single cells, for reentrant waves in a ring of cells, and for reentry in 2D sheets of ventricular tissue. We show that an important determinant for the onset of instability is the recovery dynamics of the fast sodium current. Slower sodium current recovery leads to longer periods of spiral wave rotation and more gradual conduction velocity restitution, both of which suppress restitution mediated instability. As a result maximum restitution slopes considerably exceeding one (up to 1.5) may be necessary for electrical instability to occur. Although slopes necessary for the onset of instabilities found in our paper exceed one, they are within the range of experimentally measured slopes. Therefore, we conclude that steep APD restitution mediated instability is a potential mechanism for VF in the human heart.

Keywords: reentrant arrhythmias, human ventricular myocytes, restitution properties, spiral waves, computer simulation

1 Introduction

One of the most extensively investigated hypotheses for ventricular fibrillation is the so-called restitution hypothesis. In its initial form the hypothesis stated that if the APD restitution curve has a maximum slope steeper than one, it will lead to APD alternans [41, 16]. In tissue this APD alternans can result in the fragmentation of a spiral wave leading to fibrillation like excitation patterns [45, 21, 22, 48]. Modeling studies have confirmed that a steep restitution curve indeed promotes instability. However, modeling studies have also shown that the criterium of an APD restitution slope larger than one is an oversimplification that only holds for very simple models. In more realistic and complex models it has been shown that other factors such as short term cardiac memory, electrotonic interactions between cells, conduction velocity restitution, the range of diastolic intervals over which restitution is steeper than one, and the range of diastolic intervals visited during spiral wave rotation, all play an important role in determining whether or not alternans and spiral breakup will occur [42, 48, 5, 7, 10, 11, 64]. In an extensive study of restitution induced instability Cherry and Fenton [6] for example showed that due to strong electrotonic interactions and gradual CV restitution, spiral breakup may not occur even if the APD restitution curve has slope as much as 2.

The restitution hypothesis has promoted a large number of experimental studies. An important goal of these studies was to measure restitution curves and their slopes. Experiments in animal hearts have shown that the maximum slope of the restitution curve can indeed be larger than one, for example for pig heart slopes of 1.29 [27], for dog heart slopes of 1.13 [25] and for rabbit heart slopes of 1.3 [18] up to 2.3 [2] were found. However, slopes less than one have also frequently been reported [27, 18]. In experiments it was also found that other factors

than mere APD restitution slope are important in determining whether alternans or fibrillation occurs. Wu et al. [66] and Banville and Gray [2] showed that whether or not VF occurred depended both on APD and CV restitution. Banville et al. [1] also demonstrated that cardiac memory effects play a role in whether alternans and VF occurs.

Early studies of APD restitution in the human heart suggested that the maximum slope in humans could be close to or slightly larger than one [37, 59]. More recently Pak et al. [43] measured human APD restitution in the right ventricular apex and outflow tract. They found that restitution slopes can be considerably steeper than one, reporting values of up to 1.28 for the apex and of up to 3.78 for the outflow tract. In addition they found a positive correlation between arrhythmia inducibility and both steepness and dispersion of the restitution slopes. Yue et al. [67] measured restitution on the left and right ventricular endocardium at 32 sites, reporting restitution slopes varying from site to site and ranging from zero to two. The most extensive study on human APD restitution has recently been performed by Nash et al. [38, 40, 39]. They measured restitution at 256 points covering the complete ventricular epicardium of 14 patients, showing that restitution is distributed heterogeneously but is regionally organized over the epicardial surface, with maximum slopes varying from almost zero to over three, and a mean value of 1.1.

These recent data imply the possibility of steep restitution induced instabilities in human cardiac tissue. However, as was mentioned above, the question of whether such instabilities actually do occur also depends on other factors, such as CV restitution, electrotonic interactions and cardiac memory, range of diastolic intervals over which the curve is steep, and diastolic intervals visited during spiral wave rotation. Because of the substantial limitations to

experimental studies involving human cardiac tissue, alternative methods are of great interest. In this article we will investigate the conditions for electrical instability in human ventricular tissue using the method of mathematical modeling.

For this purpose we developed an new version of our human ventricular cell model [61]. The new model is based on recent experimental restitution data [39] and incorporates an improved description of intracellular calcium dynamics, by including subspace calcium dynamics that controls L-type calcium current and calcium induced calcium release, by modeling CICR with a four-state Markov model for the Ryanodine receptor, and by incorporating both fast and slow voltage gated inactivation of the L-type calcium current. We use our new model to study the onset of alternans in a single cell, for waves propagating in a ring of cardiac tissue (a model for reentry around a fixed path) and for 2D reentry (spiral waves).

In our earlier study, we found that the recovery dynamics of the fast sodium current are considerably slower than what is often assumed in other modeling studies. Sodium current dynamics is an important determinant of conduction velocity restitution and of spiral wave rotation speed. Cherry and Fenton have demonstrated that CV restitution plays an important role in the occurrence of electrical instability [6], whereas we have previously shown that the speed of spiral wave rotation and hence the diastolic intervals visited during spiral wave rotation influence whether or not alternans instability occurs [63].

Therefore, we focus on the effect of I_{Na} recovery dynamics in combination with APD restitution on alternans and spiral breakup. In particular, we use our new model to reproduce a representative range of the experimentally measured restitution curves recently reported by

Nash et al. [39], with slopes varying from 0.7 to 2. We combine these different restitution slopes with three types of I_{Na} current recovery dynamics: slow, medium and fast recovery. We find that slower I_{Na} recovery dynamics suppresses steep APD restitution mediated instability and spiral breakup. Under slow I_{Na} recovery dynamics maximum restitution slopes significantly steeper than one are required to generate electrical instability and breakup. However, such slopes are within the range of restitution slopes reported by Nash et al. [39]. Therefore, we conclude that steep restitution mediated alternans and spiral breakup may exist in the human heart.

2 Materials and Methods

2.1 Model development

We developed a new version of our human ventricular cell model. In this new model we included a more extensive description of intracellular calcium handling, incorporating a subsarcolemmal space, describing CICR with a Markov-state model for the Ryanodine receptor, including both fast and slow voltage inactivation for the L-type calcium current, and applying some minor changes to parameter values and to slow delayed rectifier time dynamics. Important changes are discussed in detail below. Detailed equations can be found in the appendix, the new default parameter setting of our model can be found in Table 1.

2.1.1 Calcium dynamics (Ca_{ss})

A schematic representation of the calcium dynamics in our new model is given in Figure 1. The model now contains a description of calcium dynamics in the subspace (Ca_{SS}), cytoplasm (Ca_i) and sarcoplasmic reticulum (Ca_{SR}). Calcium in the subspace is buffered and a diffusion flux is added to allow calcium released in the subspace to flow to the bulk cytoplasm. L-type calcium current and the Ryanodine calcium release current now inject calcium into the subsarcolemmal subspace, and, in turn, their dynamics are influenced by the subspace calcium concentration. I_{pCa}, I_{bCa} and I_{NaCa} still depend on bulk cytoplasmic calcium.

Figure 2 shows a steady state 1Hz epicardial action potential for the new version our human ventricular cell model (A) together with the calcium transients occurring in the subspace (B) and bulk cytoplasm (C). It can be seen that the calcium transient in the subspace is much larger (peak amplitude of 1.77 versus 0.0013mM), faster (time to peak $\sim$2 versus $\sim$35ms) and shorter (duration of $\sim$35 versus $\sim$400ms) than that in the cytoplasm. Maximum upstroke velocity of the AP is 289mV/ms, the plateau level is 24.9mV and resting membrane potential is -85.8mV, all very similar to the previous version of our model. However, action potential duration (APD_{90}) now is 306ms, and was 276ms in the previous version of our model. We decided for this change to let our model APD lie more in the midrange of experimentally recorded APDs in single cell (336ms, 298ms, 360ms, 310ms [31, 30, 29, 28]) and tissue preparations (351ms, 378ms [8, 9, 14]).

2.1.2 L-type calcium current (I_{CaL})

L-type calcium current (see equation (6) of the Appendix) now injects calcium into the subspace and in turn is inactivated by the calcium in the subspace (Ca_{SS}) via the inactivation gate f_{cass} (Figure 3A and B). I_{CaL} voltage clamp experiments indicate the presence of both a fast and slow voltage dependent recovery process [35, 32, 46]. Therefore, we incorporate both a slow voltage inactivation gate f and a fast voltage inactivation gate f_2, similar to the approach taken by Hund and Rudy [19]. Figure 3C shows the steady state inactivation curves of f and f_2 and Fig. 3D shows the time constant curves of f and f_2 together with experimental data. Note that the inactivation rate of f_2 is slower than that of f_{cass} but much faster than that of f. Note also, that as opposed to the f gate, but similar to the f_{cass} gate the f_2 gate inactivates incompletely. These two properties enable the f_2 gate to take over initial inactivation from f_{cass}, which is necessary since the short duration of the subspace calcium transient leads to recovery of f_{cass} during the action potential. In Figure 3E we show the voltage dependence of our new L-type calcium current together with experimental data, demonstrating a good agreement between model and experiment [34].

2.1.3 Calcium induced calcium release (I_{rel})

In our new model we use a reduced version of the Markov-state Ryanodine receptor model developed by Shannon et al. [54] and Stern et al. [57], to describe calcium induced calcium release. Figure 4A shows the original four state Markov model of the Ryanodine receptor developed by Shannon et al. and Stern et al. It can bee seen that the model incorporates both the influence of subspace calcium concentration (the trigger) and on sarcoplasmic reticulum

calcium concentration (the load) on receptor opening and closing dynamics by making transition rates depend on these concentrations.

For computational efficiency we reduced the dimensionality of the Markov model using quasi steady state assumptions to the following set of equations:

$$\frac{d\bar{R}}{dt} = -k_2 Ca_{SS}\bar{R} + k_4(1-\bar{R}) \quad (1)$$

$$O = \frac{k_1 Ca_{SS}^2 \bar{R}}{k_3 + k_1 Ca_{SS}^2} \quad (2)$$

$$I_{rel} = V_{rel} O(Ca_{SR} - Ca_{SS}) \quad (3)$$

where $\bar{R} = R + O$, with R the resting closed state and O the open conducting state.

We determined the gain function for the dependence of calcium release on SR calcium load. (Gain is defined as the calcium induced calcium release flux normalized by the L-type calcium current flux triggering it.) Figure 4B shows gain in our model as a function of free calcium in the sarcoplasmic reticulum. For qualitative comparison experimental data from Shannon et al. [53] in rabbit ventricular myocytes are added, unfortunately we could not find data on the gain function in human ventricular myocytes. We can see that our model generates a non-linear response function, as is the case for the experimental data.

2.2 Numerical methods

Action potential generation in single cells was described using the following differential equation: [23]:

$$C_m \frac{dV}{dt} = I_{ion} + I_{stim} \quad (4)$$

where C_m is the membrane capacitance, V is the transmembrane potential, I_{stim} is the externally applied transmembrane current, and I_{ion} is the sum of all transmembrane ionic currents. For I_{ion} we use our new version of the human ventricular cell model.

Similarly, action potential generation and propagation in one dimensional cables and rings and two dimensional sheets of cardiac tissue was described using the following parabolic reaction diffusion equation [23]:

$$C_m \frac{\partial V}{\partial t} = I_{ion} + I_{stim} + \nabla D \nabla V \tag{5}$$

where D is a tensor describing the conductivity of the tissue and ∇ is the one or two-dimensional gradient operator. In one dimension $D = 0.00154 cm^2/ms$, in two dimensions $D_{ij} = 0.00154 cm^2/ms$ for $i = j$ and $D_{ij} = 0 cm^2/ms$ for $i \neq j$. With these values we obtain a maximum planar conduction velocity (CV) of $68 cm/s$ which is the velocity found for conductance along the fiber direction in human myocardium [60].

Physical units used in our model are as follows, time (t) in milliseconds, voltage (V) in millivolts, current densities (I_X) in picoamperes per picofarad, and ionic concentrations (X_i, X_o) in millimoles per liter.

For single cell simulations, forward Euler integration with a time step of $\Delta t = 0.02 ms$ was used to integrate equation 4. For 1D and 2D computations, the forward Euler method was used to integrate Equation 5 with a space step of $\Delta x = 0.25 mm$ and a time step of $\Delta t = 0.02 ms$. In all cases the Rush and Larsen integration scheme [52] was used to integrate the Hodgkin-Huxley type equations for the gating variables of the various time dependent currents (m, h and j for

I_{Na}, r and s for I_{to}, x_{r1} and x_{r2} for I_{Kr}, x_s for I_{Ks}, d, f, $f2$ and f_{cass} for I_{CaL}).

We measure action potential duration (*APD*) at either 50% or 90% repolarization and will refer to these values as APD_{90} and APD_{50} respectively. APD_{90} values will be used, unless stated otherwise. APD_{50} values are used to allow comparison between experimental activation recovery interval (*ARI*) data obtained by Nash et al. [38, 40, 39]. It has been shown that *ARI* (measured as the interval from the minimum dV/dt during the QRS wave to the maximum dV/dt of the T-wave) typically corresponds with action potential duration of around 50% repolarization [17].

In single cells, we apply both the standard S1-S2 and the dynamic protocols to determine action potential duration restitution. For the S1-S2 protocol, 10 S1 stimuli are applied at a specified basic cycle length (*BCL*) followed by a single S2 extra-stimulus delivered at some diastolic interval (*DI*) after the AP generated by the last S1 stimulus. An APD restitution curve is generated by decreasing DI and plotting the APDs generated by the S2 stimuli against the preceding DIs. In this paper, we use $BCL = 600ms$ to allow comparison with the experimental studies of Nash et al. [39]. For the dynamic restitution protocol a series of 50 stimuli is applied at a specified *BCL*, following which cycle length is decreased. The APD restitution curve is obtained by plotting the final APD for each *BCL* against the final DI.

In cables we apply the dynamic restitution protocol to determine both dynamic APD restitution and conduction velocity (*CV*) restitution. We do so by pacing one end of the 800 cells long cable at a certain *BCL* until a steady state APD and CV are reached, after which the cycle length is decreased. In rings APD and CV restitution can be obtained in the absence of external pacing. Here the restitution protocol is started by applying a single external stimulus

generating a wave that is allowed to propagate only in one direction and that will result in the repeated rotation of a wave along the ring. The cycle length of excitation is determined by the ring length. APD and CV can be determined as a function of ring length and hence cycle length and diastolic interval. We start with a ring of 1400 cells (35cm) and stepwise reduce it's length to decrease cycle length and hence obtain a restitution curve.

We use two dimensional tissue sheets of 1000×1000 cells (space step $\Delta x = 0.25mm$). In 2D spiral waves are generated by first applying a S1 stimulus producing a planar wavefront propagating in one direction, then, when the refractory tail of this wave crosses the middle of the medium, a S2 stimulus is applied generating a second wavefront perpendicular to the first. This produces a second wavefront with a free end around which it curls, forming a spiral wave. Stimulus currents lasted for 2 (S1) and 5 (S2) ms and were twice the diastolic threshold.

Single cell, cable and ring simulations were coded in C^{++} and run on a single processor of a Dell 650 Precision Workstation (dual Intel xeon 2.66 GHz). Two dimensional simulations were coded in C++ and MPI and were run on 20 processors of a Beowulf cluster consisting of 14 Dell 650 Precision Workstations (dual Intel xeon 2.66 GHz).

3 Results

3.1 APD restitution properties of human ventricular cell model

Our new model reproduces a representative range of restitution curves recently reported by Nash et al. [38, 40, 39]. Figures 5A, B, C and D show restitution curves for four different parameter settings of our model together with four different experimental restitution curves of

Nash et al. Experimental and model restitution curves were obtained using a S1S2 protocol at a BCL of 600ms. In experiments ARIs (activation recovery intervals) were measured, which correspond to APD50 (see methods). Model restitution curves are plotted for both APD50 and APD90 levels. Note that there is good agreement between experimental and model curves for diastolic intervals of 200ms and smaller, i.e. for diastolic intervals that determine the maximum slope of the restitution curve and that determines the onset of instability. For this study we use four parameter settings corresponding to four different slopes of the restitution curves. For setting 1 the maximum restitution slope (S_{max}) is 0.7 (5A); for setting 2 it is 1.1 (5B); for setting 3 it is 1.4 (5C); and for setting 4 it is 1.9 (5D). Table 1 lists the complete default parameter setting and Table 2 lists the parameter values varied to obtain these different restitution slopes.

3.2 Conditions for alternans in human ventricular tissue

3.2.1 Restitution and alternans in single cells

It has been suggested by Koller et al. [25] that the slope of the dynamic restitution curve is a better predictor for alternans instability than that of the S1S2 restitution curve. Therefore we also determined dynamic restitution for our four different model settings. Figures 5E, F, G and H show restitution curves obtained using a dynamic restitution protocol and measuring APD at 90% repolarization. Maximum restitution slopes for our four setting are now 0.8 (5E), 1.1 (5F), 1.4 (5G) and 1.8 (5H), respectively. This agrees with experimental data from Pak et al. [43] who demonstrated similar maximum slopes for S1S2 and dynamic restitution in the human ventricles.

In Figures 5I, J, K and L, we show APD restitution for the same dynamic restitution

protocol, but now with APD plotted versus period. We can see that for setting 1 (5I) no alternans occurs. For setting 2 (5J) APD alternans occurs, resulting in the splitting of the restitution curve in an upper and lower arm representing the long and short action potentials. Alternans occurs for periods between 236ms and 182ms, corresponding to DIs between 51 and 24ms for which the slope of the restitution curve in Fig. 5F exceeds one. Alternans reaches a maximum amplitude of 48ms at a period of 226ms and then decreases in amplitude and disappears for periods smaller than 182ms, qualitatively similar to what occurs in the model of Fox et al. [12]. For setting 3 (5K) APD alternans occurs for periods smaller than 280ms, corresponding to DIs$<$74ms for which restitution slope in Fig. 5G > 1, and reaches a maximum amplitude of 100ms. For setting 4 (5L) alternans occurs for BCL of 320ms and smaller, corresponding to DIs$<$94ms for which slope in Fig. 5H > 1, and reaches a maximum amplitude of 162ms. Our finding that alternans amplitude increases with restitution slopes is consistent with experimental results [26, 24].

3.2.2 Restitution and alternans in a ring

The occurrence of alternans in a single cell does not necessarily imply that alternans and spiral breakup occurs in tissue. In tissue additional factors besides action potential duration restitution, such as electrotonic interactions and conduction velocity restitution, the range of diastolic intervals for which restitution is steep, the range of diastolic intervals visited during spiral wave rotation all play a role in determining whether alternans occurs [42, 48, 5, 7, 10, 11, 64, 6].

In our previous study [61] we found that recovery of inactivation of human cardiac fast

sodium channels, is considerably slower than that of the phase one Luo-Rudy model [33], which is used in many cardiac tissue models. I_{Na} dynamics may effect period of spiral wave rotation, conduction velocity restitution and spiral wave meander pattern, all of which are known to effect the occurrence of alternans instability. Therefore, in tissue simulations, we investigate the combined effect of APD restitution and sodium current recovery dynamics on dynamical instability. To do so we considered three different descriptions for the fast sodium current dynamics: the default formulation of our model [61], (referred to as standard I_{Na} setting); an I_{Na} formulation using m, h and j gate dynamics as in the phase one Luo-Rudy model [33] (referred to as the LR I_{Na} setting); and an intermediate setting. The intermediate setting is similar to the standard I_{Na} setting, except that $\tau_{j,intermediate} = 0.5 \times \tau_{j,standard}$. Note, that changes in our model's fast I_{Na} dynamics have virtually no effect on the single cell APD restitution properties shown in Fig.5.

To examine the combined effect of APD restitution properties and I_{Na} recovery dynamics on the occurrence of electrical instability in tissue we combined the four different APD restitution parameter settings with the three different I_{Na} dynamics discussed above. This resulted in a total of 12 different model settings. Using these settings we studied the stability of wave propagation in a ring, which is a 1D model for reentry along a fixed path. Note that it was shown in [6] that the conditions for instability in a ring are the same as the conditions for spiral breakup in 2D tissue.

In Figure 6 we show action potential duration as a function of period in the 12 different model settings for a wave circulating on a ring. Figure 6A shows restitution for parameter setting 1 ($S_{max} = 0.7$) combined with either the standard, intermediate or LR sodium current

dynamics (curves are superimposed). We can see that for none of these settings alternans occurs. The sodium current dynamics however does affect the period for which block occurs: for standard I_{Na} dynamics block occurs for periods smaller than 216ms, for intermediate dynamics block occurs for periods smaller than 202ms, and for LR dynamics block occurs for periods smaller than 170ms. In Figure 6B we can see that setting 2 ($S_{max} = 1.1$) for standard and intermediate I_{Na} dynamics no alternans occurs, but for LR sodium dynamics alternans occurs for periods between 255 and 170ms, with a maximum amplitude of 25ms.

In Figure 6C we see that for setting 3 ($S_{max} = 1.4$), no alternans occurs for standard sodium current dynamics. Both the intermediate and LR dynamics result in alternans. For intermediate sodium dynamics alternans occurs for periods smaller than 280ms, with a maximum amplitude of around 50ms, for LR sodium dynamics alternans occurs for periods smaller than 300ms, with a maximum amplitude of around 90ms. Finally, in Figure 6D we see that for parameter setting 4 ($S_{max} = 1.9$) alternans occurs in all three cases. For the standard dynamics alternans occurs for periods smaller than 321ms, and for the intermediate and LR settings for periods smaller than 330ms. Maximum alternans amplitude increased from around 75ms to 125ms and to 150ms when going from standard to intermediate to LR sodium current dynamics.

Our results show that for fast (LR) sodium current dynamics, alternans instability occurs for the same APD restitution slopes in a single cell as in a ring of tissue. For slow (standard) and intermediate sodium current dynamics this is not the case. For standard and intermediate sodium current dynamics a steeper APD restitution slope is required in a ring than in a single cell to generate alternans. These results suggest that faster sodium recovery dynamics lead to earlier occurrence and larger amplitude of alternans, and that slower sodium recovery

suppresses alternans.

3.2.3 Spiral wave dynamics and alternans in a plane

In Figure 7 we show snapshots of spiral wave dynamics for the 12 different model settings that we studied in the previous section. The three columns represent the three different sodium current dynamics (standard, intermediate, LR). The four rows represent the four different parameter settings resulting in the four different APD restitution slopes. If spiral breakup occurs, the time of first wave break is indicated in the top left corner. Spiral wave dynamics were simulated for 4s. If no spiral breakup occurred in this time frame spiral wave dynamics was assumed to be stable.

We can see that for parameter setting 1 ($S_{max} = 0.7$, first row) stable spiral wave dynamics occur for all three sodium current dynamics. For setting 2 ($S_{max} = 1.1$, second row) spiral wave dynamics is stable for the standard and intermediate sodium dynamics, but for the LR dynamics spiral breakup occurs after 1.17s. For parameter setting 3 ($S_{max} = 1.4$, third row) spiral wave dynamics is only stable for the standard I_{Na} dynamics. For the intermediate dynamics spiral breakup occurs after 2s, while for the LR dynamics breakup occurs after 0.72s. For setting 4 ($S_{max} = 1.9$, fourth row) spiral breakup occurs for all three sodium current dynamics. For the standard sodium dynamics breakup occurs after 2.16s, for the other two sodium dynamics breakup occurs after 1.44s.

The conditions we find for spiral breakup in 2D correspond nicely with the conditions we find for alternans in a ring. Using some extra parameter settings resulting in restitution slopes in between the 1.4 and 1.9 we used here, we found that the occurrence of alternans/spiral breakup

under standard sodium recovery required a minimum APD restitution slope of 1.5 (data not shown).

3.3 How does I_{Na} dynamics affect instability?

From the previous sections we conclude that for LR sodium current dynamics in our model a slope just over one (1.1) suffices to generate alternans and spiral breakup, whereas for the standard sodium current dynamics in our model a slope of 1.5 is required to generate alternans and spiral breakup. This implies that slow sodium current recovery dynamics suppresses alternans instability and breakup. Figure 8 shows the effect of I_{Na} dynamics on two factors that have been shown to be important for alternans instability: CV restitution and the diastolic intervals visited during spiral wave rotation.

Figure 8A shows 3 CV restitution curves generated with our model for the three different I_{Na} dynamics. We can see that the standard I_{Na} dynamics results in a CV restitution curve that starts gradually declining for DIs of 250ms and smaller. The LR sodium current dynamics result in a CV restitution curve that is nearly flat for a broad range of diastolic intervals and then declines fast for DIs smaller than 65ms. We can see that the intermediate sodium current dynamics indeed result in an intermediate CV restitution curve. It has been shown in both analytical and modeling studies that a shallow CV restitution curve suppresses alternans and spiral breakup [10, 7, 6]: in tissue, through electrotonic interactions, gradual CV restitution increases the threshold value for APD restitution slopes above which instability occurs above one.

Figure 8B shows periods and diastolic intervals visited during spiral wave rotation for the

three different sodium current dynamics. For illustration purposes, we did this for parameter setting 1 (restitution slope<1) to ensure stable spiral wave rotation for all sodium dynamics. We can see that when going from standard to intermediate to LR sodium dynamics both period and diastolic interval decrease. It is a well known effect that slowing of spiral wave rotation leads to stabilization. We found in our earlier studies that the mechanism behind this stabilization is that for slower sodium recovery and hence longer periods and diastolic intervals a less steep part of the restitution curve is visited, thus supressing alternans and spiral breakup [44, 62, 63].

Is it the shallower CV restitution, or the longer diastolic interval during spiral wave rotation, or both that leads to suppression of instability? We tried to resolve this issue by changing diastolic interval, while keeping the shape of the CV restitution curve the same. This can be achieved by changing maximal conductance G_{Na} of the sodium current. Table 3 shows period and diastolic intervals of spiral wave rotation for parameter setting 1, either our standard or LR sodium current dynamics and different G_{Na}. From the table we can see that DI can be reduced from 32ms -occurring for standard sodium dynamics- to 22ms -close to the DI for LR I_{Na} dynamics- by increasing G_{Na} with a factor 7. Similarly, we can increase DI from 19ms -occurring for the LR sodium current dynamics- to 29ms -close to the DI for standard I_{Na} dynamics- by multiplying G_{Na} with a factor of 0.4. Note, that although the CV restitution curve will shift as a result of these modifications, its shape will be maintained (not shown). Furthermore, we assume that multiplication of G_{Na} by these factors will also work for the other parameter setting of our model.

We simulated spiral wave dynamics for parameter settings 2 and 3 (slope 1.1 and 1.4,

respectively) either using our standard sodium current dynamics combined with $G_{Na} \times 7$, or using LR sodium current dynamics combined with $G_{Na} \times 0.4$. We see (Figure 9B) that for setting 2 only increasing DI for LR I_{Na} dynamics suffices to remove spiral breakup, thus we obtain the same spiral wave dynamics as for our standard I_{Na} dynamics. Similarly, Figure 9C shows that for setting 3 decreasing DI for standard sodium current dynamics induces spiral breakup, thus resulting in the same spiral wave dynamics as for LR I_{Na} dynamics. These two simulations thus suggest that changes in *DI* alone can explain the effects of the different I_{Na} dynamics on alternans and spiral wave stability observed in this paper. However, our other simulation results do not support this conclusion: For setting 2 decreasing DI for standard sodium current dynamics does not result in the onset of spiral breakup, as observed for LR I_{Na} dynamics, however, it does result in transient initial wave breaks (Fig. 9A). For setting 3 increasing DI for LR I_{Na} does not prevent spiral breakup (Fig. 9D), as expected from computations for standard I_{Na} dynamics. Therefore, we conclude that although the diastolic intervals visited during spiral wave rotation have a pronounced effect on the onset of alternans and spiral breakup, conduction velocity restitution also plays an important role in determining whether or not instability will occur.

4 Discussion

New version of human ventricular cell model

In this paper we developed a new version of our human ventricular cell model. In the new model we incorporated a subspace calcium variable that controls the dynamics of the L-type

calcium current and the Ryanodine receptor current. Similar approaches have been taken in many recent models [20, 19, 54]. In addition we changed the gating dynamics of I_{CaL}, which now has a fast subspace calcium inactivation gate f_{cass}, and a slow and fast voltage inactivation gate f and f_2, resulting in L-type calcium current dynamics that agree better with experimental data. We have also replaced the phenomenological, description of CICR in our previous model with a reduced version of the Ryanodine receptor Markov model developed by Stern et al. [57] and Shannon et al. [54]. We demonstrated that with this new description our model is able to reproduce a non-linear gain function for calcium release as a function of SR calcium load.

Although we improved the description of calcium handling in this new version of our model, our formulation is still a simplification and cannot describe all details of calcium dynamics. For example, to describe gradedness of CICR much more complex models incorporating the description of individual L-type channels, Ryanodine receptors, etcetera are necessary [51, 15]. However, such models are computationally very demanding and therefore not feasible for modeling cardiac tissue sheets or complete ventricles, for which our model is intended.

Conditions for alternans and spiral breakup

We use our new model to study the conditions under which electrical instability and spiral breakup occur, to establish whether the spiral breakup hypothesis of VF can be valid for human ventricular tissue. We focus both on the role of APD restitution, reproducing a representative range of recently measured human ventricular restitution curves from Nash et al. [39], and on the role of the recovery dynamics of the fast sodium current, of which we found in our previous study that it is much slower than as previously assumed in a lot of cardiac tissue modeling

studies [61].

We find that for fast (LR) sodium current recovery dynamics, an APD restitution slope just over one (1.1) is enough to result in alternans in single cells and rings of cells and to generate spiral breakup in 2D sheets of tissue. For slower (standard and intermediate) sodium current recovery dynamics, steeper APD slopes are required to get electrical instability in rings and sheets of tissue.

These findings imply that slow sodium current recovery dynamics has a protective effect against steep APD restitution mediated instability and spiral breakup. This may be an important finding, given that alternans and breakup are most often studied in models with a fast (LR) sodium current dynamics. As we demonstrated earlier [61], voltage clamp data for human cardiac fast sodium channels show slow sodium current recovery dynamics. Here we find that for the standard sodium current dynamics of our model, which are based on these experimental data, an APD restitution slope significantly steeper than one -for our particular settings 1.5- is needed to generate spiral breakup. This 1.5 is well within the range of experimentally found values [43, 38, 40, 39]. Therefore, our results do support that steep APD restitution mediated instability is a potential mechanism for VF in the human heart.

Mechanism of breakup suppression

Slow I_{Na} dynamics lead both to longer periods and diastolic intervals of spiral wave rotation (Fig. 8B) and a more gradual CV restitution curve (Fig. 8A). We performed a qualitative study of the relative importance of diastolic interval during spiral wave rotation and more gradual CV restitution for the suppression of instability, by isolating the CV effect and compensating for the diastolic interval effect of the different I_{Na} dynamics using I_{Na} conductance. We found that

in some cases the DI effect can explain differences in spiral breakup or no spiral breakup for the different sodium current dynamics. However, for other parameter settings differences in spiral wave stability could not be explained merely by the DI effect. This suggests that spiral wave period is not the only important effect of slower I_{Na} current recovery that leads to alternans suppression, and that the conduction velocity effect also plays a role in suppressing instability. Unfortunately we found no way to change CV restitution shape while keeping the DI of spiral wave rotation constant to further establish the precise importance of CV restitution versus DI.

Relation to work of others

In analytical studies it was shown that for waves propagating in tissue, the condition for steep restitution mediated alternans instability was not simply slope<1 but is slope $< 1+\xi c^{'}/c^2$ [10, 7]. Here ξ represents the strength of action potential morphology (especially repolarization wave back) dependent electrotonic interactions, $c^{'}$ the derivative of the conduction velocity curve for the relevant diastolic interval (i.e. that of rotation on a ring or spiral wave rotation) and c the maximum planar conduction velocity. From the formula it follows that the larger the value of ξ (stronger electrotonic interactions) and the larger the value of $c^{'}/c^2$ (large change of CV over range of DIs or low conduction velocity), the steeper a slope is required to generate instability. Here we indeed found that the slower the sodium current recovery dynamics, and hence the more gradual the CV restitution curve, the steeper an APD restitution slope was needed to generate instability. Our results agree with a previous study from Qu et al. [48], who showed that a CV restitution curve that stays flat over a broad range of DIs, similar to our steep CV curve, promotes spiral breakup, and to results from Fox et al. [13], who showed that chances of conduction block decrease for lower CVs at short cycle lengths, corresponding

to our more gradual CV restitution. Our results also agree with results from an extensive simulation study on the dependence of alternans and spiral breakup on APD restitution, CV restitution, electrotonic interactions and cardiac memory performed by Cherry and Fenton [6]. They found that for action potentials with a fast repolarizing wave back -leading to strong electrotonic interactions- a more gradual CV restitution can suppress alternans in a ring and spiral breakup in 2D. Note that in our human ventricular cell model we have a strong repolarizing wave back caused by the large I_{K1} current.

Our results may seem dissimilar from results such as those of Cao et al. and Watanabe et al. [5, 65] who showed that a more gradual CV restitution is pro-arrhythmic because it promotes the spatial discordance of alternans, causing spiral breakup to require a smaller tissue size. However, as it was noted by Cherry and Fenton [6] gradual CV restitution has a dual effect: on one hand it can suppress alternans provided that electrotonic interactions are strong, on the other hand it promotes the spatial discordance of any alternans still present. Whether or not alternans arises thus depends on the strength of electrotonic interactions, the shape of CV restitution, and tissue size. In our model we found in the 2D sheets of tissue of 20×20cm only the alternans suppressing effect. This suggests that a larger tissue size is needed for discordant alternans to develop. Given that 20×20cm is large relative to human heart size, we conclude that for the human ventricles and standard sodium current dynamics, the alternans suppressing effect will dominate.

The results we found here also agree with previous work from our group [44, 62, 63]. In these studies we found that the presence of inexcitable obstacles or the removal of gap junctional connections between cells lead to suppression of spiral breakup. This suppression

was caused by the slowing down of spiral wave rotation, leading to longer diastolic intervals, similar to the effect of slower fast sodium current recovery. Longer diastolic intervals shift the position of the spiral wave on the (unchanged) restitution curve to the right and upward, away from the steepest part.

Limitations

The ionic mechanisms responsible for the variation in APD restitution curves are currently unknown. In this paper, to obtain different restitution slopes, we used more general knowledge of the influence of certain parameters on APD and APD restitution. We varied the dynamics of the L-type calcium current, as it has been shown in both modeling studies [49, 12] and experiments [50] that I_{CaL} is a major determinant of restitution slope. Action potential duration was then readjusted by varying conductances of I_{Kr}, I_{Ks}, I_{pCa} and I_{pK} (Table 2). If new data on the ionic current differences underlying restitution variation become available, new parameter settings based on these data need to be constructed. However, we expect that restitution slope rather than the parameter setting is important for the observed effects and hence that results will stay similar.

In this study we find that a slow I_{Na} recovery dynamics protects against steep APD restitution mediated alternans. However, we investigated this in homogeneous rings and sheets of cardiac tissue, whereas real cardiac tissue is heterogeneous in numerous properties including APD and APD restitution [43, 39], is anisotropic and has a complex anatomy. It therefore remains to be investigated what are the precise conditions for spiral breakup under more realistic conditions. In addition, we did not investigate the influence of the amount of electrotonic coupling and cardiac memory on the conditions for alternans and spiral breakup.

Furthermore, the steep APD restitution we studied here is not the only mechanism that can lead to alternans instability. Other instabilities, for example in the intracellular calcium dynamics [56, 47, 55], can lead to action potential alternans. Finally, other mechanisms than alternans leading to spiral breakup have been suggested to underly ventricular fibrillation, for example the mother rotor hypothesis (ref).

Conclusion

We propose a novel model for human ventricular cells. We report that sodium current recovery dynamics plays an important role in the occurrence of steep restitution mediated dynamical electrical instability. The slow recovery dynamics found in experiments on human cardiac sodium current suppress electrical instability. We conclude that steep restitution mediated fibrillation can occur in human ventricular tissue. However, an action potential duration restitution slope considerably steeper than one is required.

5 Acknowledgments

We would like to thank Dr. J. Sneyd, Dr. M. Nash and Dr. P. Taggart for valuable discussions. This work was supported by the Netherlands Organization for Scientific Research (NWO) through grant number 635100004 of the Research Council for Physical Sciences (EW) (K.H.W.J. ten Tusscher).

6 Appendix

No changes were made to formulations of the following currents: I_{Na}, I_{to}, I_{Kr}, I_{K1}, I_{NaCa}, I_{NaK}, I_{pCa}, I_{pK}, I_{bNa} and I_{bCa}. For these formulations we refer to their description in the previous version of our model [61].

L-type Ca^{2+} current

$$I_{CaL} = G_{CaL} d f f_2 f_{cass} 4 \frac{(V-15)F^2}{RT} \frac{0.25 Ca_{SS} e^{2(V-15)F/RT} - Ca_o}{e^{2(V-15)F/RT} - 1} \tag{6}$$

$$d_\infty = \frac{1}{1+e^{(-8-V)/7.5}} \tag{7}$$

$$\alpha_d = \frac{1.4}{1+e^{(-35-V)/13}} + 0.25 \tag{8}$$

$$\beta_d = \frac{1.4}{1+e^{(V+5)/5}} \tag{9}$$

$$\gamma_d = \frac{1}{1+e^{(50-V)/20}} \tag{10}$$

$$\tau_d = \alpha_d \beta_d + \gamma_d \tag{11}$$

$$f_\infty = \frac{1}{1+e^{(V+20)/7}} \tag{12}$$

$$\alpha_f = 1102.5 e^{-(\frac{V+27}{15})^2} \tag{13}$$

$$\beta_f = \frac{200}{1+e^{(13-V)/10}} \tag{14}$$

$$\gamma_f = \frac{180}{1+e^{(V+30)/10}} + 20 \tag{15}$$

$$\tau_f = \alpha_f + \beta_f + \gamma_f \tag{16}$$

$$f_2\infty = \frac{0.67}{1+e^{(V+35)/7}} + 0.33 \tag{17}$$

$$\alpha_{f2} = 600 e^{-\frac{(V+25)^2}{170}} \tag{18}$$

$$\beta_{f2} = \frac{31}{1+e^{(25-V)/10}} \tag{19}$$

$$\gamma_{f2} = \frac{16}{1+e^{(V+30)/10}} \tag{20}$$

$$\tau_{f2} = \alpha_{f2} + \beta_{f2} + \gamma_{f2} \tag{21}$$

$$f_{cass\infty} = \frac{0.6}{1+(\frac{CaSS}{0.05})^2} + 0.4 \tag{22}$$

$$\tau_{fcass} = \frac{80}{1+(\frac{CaSS}{0.05})^2} + 2 \tag{23}$$

Slow delayed rectifier current

$$I_{Ks} = G_{Ks} x_s^2 (V - E_{Ks}) \tag{24}$$

$$x_{s\infty} = \frac{1}{1 + e^{(-5-V)/14}} \tag{25}$$

$$\alpha_{xs} = \frac{1400}{\sqrt{1 + e^{(5-V)/6}}} \tag{26}$$

$$\beta_{xs} = \frac{1}{1 + e^{(V-35)/15}} \tag{27}$$

$$\tau_{xs} = \alpha_{xs} \beta_{xs} + 80 \tag{28}$$

Calcium dynamics

$$J_{leak} = V_{leak}(Ca_{SR} - Ca_i) \tag{29}$$

$$J_{up} = \frac{V_{maxup}}{1 + K_{up}^2/Ca_i^2} \tag{30}$$

$$J_{rel} = V_{rel} O (Ca_{SR} - Ca_{SS}) \tag{31}$$

$$J_{xfer} = V_{xfer}(Ca_{SS} - Ca_i) \tag{32}$$

$$O = \frac{k_1 Ca_{SS}^2 \bar{R}}{k_3 + k_1 Ca_{SS}^2} \tag{33}$$

$$\frac{d\bar{R}}{dt} = -k_2 Ca_{SS}\bar{R} + k_4(1 - \bar{R}) \tag{34}$$

$$k_1 = \frac{k_{1'}}{k_{casr}} \tag{35}$$

$$k_2 = k_{2'} k_{casr} \tag{36}$$

$$k_{casr} = max_{sr} - \frac{max_{sr} - min_{sr}}{1 + (EC/Ca_{SR})^2} \tag{37}$$

$$Ca_{ibufc} = \frac{Cai \times Buf_c}{Cai + K_{bufc}} \tag{38}$$

$$dCa_{itotal}/dt = -\frac{I_{bCa} + I_{pCa} - 2I_{NaCa}}{2V_c F} + \frac{V_{sr}}{V_c}(J_{leak} - J_{up}) + J_{xfer} \tag{39}$$

$$Ca_{srbufsr} = \frac{Ca_{sr} \times Buf_{sr}}{Ca_{sr} + K_{bufsr}} \tag{40}$$

$$dCa_{SRtotal}/dt = (J_{up} - J_{leak} - J_{rel}) \tag{41}$$

$$Ca_{ssbufss} = \frac{Ca_{ss} \times Buf_{ss}}{Ca_{ss} + K_{bufss}} \tag{42}$$

$$dCa_{SStotal}/dt = -\frac{I_{CaL}}{2V_{ss}F} + \frac{V_{sr}}{V_{ss}} J_{rel} - \frac{V_c}{V_{ss}} J_{xfer} \tag{43}$$

References

[1] I. Banville, N. Chattipakorn, and R. A. Gray. Restitution dynamics during pacing and arrhythmias in isolated pig hearts. *J. Cardiovasc. Electrophysiol.*, 15:455–463, 2004.

[2] I. Banville and R. A. Gray. Effect of action potential duration and conduction velocity restitution and their spatial dispersion on alternans and the stability of arrhythmias. *J. Cardiovasc. Electrophysiol.*, 13(11):1141–1149, 2002.

[3] J. Benitah, P. Bailly, M. D'Agrosa, J. Da Ponte, C. Delgado, and P. Lorente. Slow inward current in single cells isolated from adult human ventricles. *Pflugers Arch.*, 421:176–187, 1992.

[4] D. J. Beuckelmann, M. Nabauer, and E. Erdmann. Characteristics of Calcium-Current in Isolated Human Ventricular Myocytes from Patients with Terminal Heart Failure. *J. Mol. Cell. Cardiol.*, 23:929–937, 1991.

[5] J. Cao, Z. Qu, Y. Kim, T. Wu, A. Garfinkel, J. N. Weiss, H. S. Karagueuzian, and P. Chen. Spatiotemporal Heterogeneity in the Induction of Ventricular Fibrillation by Rapid Pacing, Importance of Cardiac Restitution Properties. *Circ. Res.*, 84:1318–1331, 1999.

[6] E. M. Cherry and F. H. Fenton. Suppression of alternans and conduction blocks despite steep APD restitution: Electrotonic, memory and conduction velocity effects. *Am. J. Physiol. Heart Circ. Physiol.*, 286:H2332–H2341, 2004.

[7] E. Cytrynbaum and J. P. Keener. Stability conditions for the traveling pulse: Modifying the restitution hypothesis. *Chaos.*, 12(3):788–799, 2002.

[8] E. Drouin, F. Charpentier, C. Gauthier, K. Laurent, and H. Le Marec. Electrophysiologic characteristics of cells spanning the left ventricular wall of human heart: evidence for the presence of M cells. *J. Am. Coll. Cardiol.*, 26:185–192, 1995.

[9] E. Drouin, G. Lande, and F. Charpentier. Amiodarone Reduces Transmural Heterogeneity of Repolarization in the Human Heart. *J. Am. Coll. Cardiol.*, 32:1063–1067, 1998.

[10] B. Echebarria and A. Karma. Instability and spatiotemporal dynamics of alternans in paced cardiac tissue. *Phys. Rev. Lett.*, 88(20):208101, 2002.

[11] J. J. Fox, E. Bodenschatz, and R. F. Gilmour, Jr. Period-doubling instability and memory in cardiac tissue. *Phys. Rev. Lett.*, 89(13):138101, 2002.

[12] J. J. Fox, J. L. McHarg, and R. F. Gilmour. Ionic mechanism of electrical alternans. *Am. J. Physiol. Heart Circ. Physiol.*, 282:H516–H530, 2002.

[13] J. J. Fox, M. L. Riccio, P. Drury, A. Werthman, and R. F. Gilmour, Jr. Dynamic mechanism for conduction block in heart tissue. *New J. Phys.*, 5:101.1–101.14, 2003.

[14] R. F. Gilmour, J. J. Heger, E. N. Prystowsky, and D. Z. Zipes. Cellular electrophysiologic abnormalities of diseased human ventricular myocardium. *Am J Cardiol*, 51:137–144, 1983.

[15] J. L. Greenstein and R. L. Winslow. An Integrative Model of the Cardiac Ventricular Myocyte Incorporating Local Control of Ca^{2+} Release. *Biophys. J.*, 83:2918–2945, 2002.

[16] M.R. Guevara, A. Ward, A. Shrier, and L. Glass. Electrical alternans and period doubling bifurcations. *IEEE Comp. Cardiol.*, 562:167–170, 1984.

[17] C. W. Haws and R. L. Lux. Correlation between in vivo transmembrane action potential durations and activation-recovery intervals from electrograms. Effects of interventions that alter repolarization time. *Circulation.*, 81(1):281–288, 1990.

[18] H. Hayashi, Y. Miyauchi, C. C. Chou, H. S. Karagueuzian, P. S. Chen, and S. F. Lin. Effects of cytochalasin D on electrical restitution and the dynamics of ventricular fibrillation in isolated rabbit heart. *J. Cardiovasc. Electrophysiol.*, 14(10):1077–1084, 2003.

[19] T. J. Hund and Y. Rudy. Rate dependence and regulation of action potential and calcium transient in a canine cardiac ventricular cell model. *Circulation.*, 110(20):3168–3174, 2004.

[20] V. Iyer, R. Mazhari, and R.L. Winslow. A computational model of the human left-ventricular epicardial myocyte. *Biophys. J.*, 87:1507–1525, 2004.

[21] A. Karma. Spiral breakup in model equations of action potential propagation in cardiac tissue. *Phys. Rev. Lett.*, 71:1103–1106, 1993.

[22] A. Karma. Electrical alternans and spiral wave breakup in cardiac tissue. *Chaos*, 4:461–472, 1994.

[23] J. Keener and J. Sneyd. *Mathematical physiology*. Springer-Verlag, New York, Heidelberg, Berlin, 1998.

[24] M. L. Koller, S. K. Maier, A. R. Gelzer, W. R. Bauer, M. Meesmann, and R. F. Gilmour Jr. Altered dynamics of action potential restitution and alternans in humans with structural heart disease. *Circulation*, 112:1542–1548, 2005.

[25] M. L. Koller, M. L. Riccio, and R. F. Gilmour Jr. Dynamic restitution of action potential duration during electrical alternans and ventricular fibrillation. *Am. J. Physiol. Heart Circ. Physiol.*, 275:H1635–H1642, 1998.

[26] M. L. Koller, M. L. Riccio, and R. F. Gilmour Jr. Effects of [K(+)](o) on electrical restitution and activation dynamics during ventricular fibrillation. *Am. J. Physiol. Heart Circ. Physiol.*, 279:H2665–H2672, 2000.

[27] M. H. Lee, S. F. Lin, T. Ohara, C. Omichi, Y. Okuyama, E. Chudin, A. Garfinkel, J. N. Weiss, H. S. Karagueuzian, and P. S. Chen. Effects of diacetyl monoxime and cytochalasin D on ventricular fibrillation in swine right ventricles. *Am J Physiol Heart Circ Physiol*, 280:H2689–H2696, 2001.

[28] G. Li, C. Lau, Leung T., and S. Nattel. Ionic current abnormalities associated with prolonged action potentials in cardiomyocytes from diseased human right ventricles. *Heart Rhythm*, 4:460–468, 2004.

[29] G. Li, B. Yang, J. Feng, R. F. Bosch, M. Carrier, and S. Nattel. Transmembrane I_{Ca} contributes to rate-dependent changes of action potentials in human ventricular myocytes. *Am. J. Physiol. Heart Circ. Physiol.*, 276:H98–H106, 1999.

[30] G. R. Li, J. Feng, L. Yue, and M. Carrier. Transmural heterogeneity of action potentials

and I_{to1} in myocytes isolated from the human right ventricle. *Am. J. Physiol. Heart Circ. Physiol.*, 275:H369–H377, 1998.

[31] G. R. Li, J. Feng, L. Yue, M. Carrier, and S. Nattel. Evidence for Two Components of Delayed Rectifier K^+ Current in Human Ventricular Myocytes. *Circ. Res.*, 78:689–696, 1996.

[32] G. R. Li and S. Nattel. Properties of human atrial I_{Ca} at physiological temperatures and relevance to action potential. *Am. J. Physiol. Heart Circ. Physiol.*, 272:H227–H235, 1997.

[33] C. Luo and Y. Rudy. A Model of the Ventricular Cardiac Action Potential, Depolarization, Repolarization, and Their Interaction. *Circ. Res.*, 68:1501–1526, 1991.

[34] J. Magyar, N. Iost, A. Kortvely, T. Banyasz, L. Virag, P. Szigligeti, A. Varro, M. Opincariu, J. Szecsi, J. G. Papp, and P. P. Nanasi. Effects of endothelin-1 on calcium and potassium currents in undiseased human ventricular myocytes. *Pflugers Arch - Eur J Physiol*, 441:144–149, 2000.

[35] J. Magyar, N. Szentandrassy, T. Banyasz, L. Fulop, A. Varro, and P. P. Nanasi. Effects of thymol on calcium and potassium currents in canine and human ventricular cardiomyocytes. *Br. J. Pharmacol.*, 136:330–338, 2002.

[36] T. Mewes and U. Ravens. L-type Calcium Currents of Human Myocytes from Ventricle of Non-Failing and Failing Hearts and Atrium. *J. Mol. Cell. Cardiol.*, 26:1307–1320, 1994.

[37] J. M. Morgan, D. Cunningham, and E. Rowland. Dispersion of monophasic action

potential duration: demonstrable in humans after premature ventricular extrastimulation but not in steady state. *J. Am. Coll. Cardiol.*, 19:1244–1253, 1992.

[38] M. P. Nash, C. P. Bradley, P. Sutton, M. Hayward, D. J. Paterson, and P. Taggart. Human hearts possess large regions of steep and flat APD restitution. *Europace*, 6, S1:187, 2004.

[39] M. P. Nash, C. P. Bradley, P. M. Sutton, R. H. Clayton, P. Kallis, M. Hayward, D. J. Paterson, and P. Taggart. Whole heart APD restitution properties in cardiac patients: A combined clinical and modeling study. *Experimental Physiology*, 2006.

[40] M. P. Nash, C. P. Bradley, P. M. Sutton, M. Hayward, D. J. Paterson, and P. Taggart. Spatial heterogeneity of action potential duration restitution in humans. *Heart Rhythm*, 2 (1S):S216–S217, 2005.

[41] J.B. Nolasco and R.W. Dahlen. A graphic method for the study of alternation in cardiac action potentials. *J. Appl. Physiol.*, 25:191–196, 1968.

[42] N. F. Otani and R. F. Gilmour, Jr. Memory models for the electrical properties of local cardiac systems. *J. Theor. Biol.*, 187(3):409–436, 1997.

[43] H. N. Pak, S. J. Hong, G. S. Hwang, H. S. Lee, S. W. Park, J. C. Ahn, Y. Moo Ro, and Y. H. Kim. Spatial dispersion of action potential duration restitution kinetics is associated with induction of ventricular tachycardia/fibrillation in humans. *J. Cardiovasc. Electrophysiol.*, 15(12):1357–1363, 2004.

[44] A. V. Panfilov. Spiral breakup in an array of coupled cells: the role of the intercellular conductance. *Phys. Rev. Lett.*, 88:118101–1–118101–4, 2002.

[45] A. V. Panfilov and A. V. Holden. Self-generation of turbulent vortices in a two-dimensional model of cardiac tissue. *Phys. Lett. A*, 147:463–466, 1990.

[46] B. Pelzmann, P. Schaffer, E. Bernhart, P. Lang, H. Machler, B. Rigler, and B. Koidl. L-type calcium current in human ventricular myocytes at a physiological temperature from children with tetralogy of Fallot. *Cardiovasc. Res.*, 38:424–432, 1998.

[47] E. J. Pruvot, R. P. Katra, D. S. Rosenbaum, and K. R. Laurita. Role of calcium cycling versus restitution in the mechanism of repolarization alternans. *Circ. Res.*, 94:1083–1090, 2004.

[48] Z. Qu, J. N. Weiss, and A. Garfinkel. Cardiac electrical restitution properties and stability of reentrant spiral waves: a simulation study. *Am. J. Physiol. Heart Circ. Physiol*, 276:H269–H283, 1999.

[49] Z. Qu, F. Xie, A. Garfinkel, and J. N. Weiss. Origins of spiral wave meander and breakup in a two-dimensional cardiac tissue model. *Ann. Biomed. Eng.*, 28(7):755–771, 2000.

[50] M. L. Riccio, M. L. Koller, and R. F. Gilmour, Jr. Electrical restitution and spatiotemporal organization during ventricular fibrillation. *Circ. Res.*, 84(8):955–963, 1999.

[51] J. J. Rice, M. S. Jafri, and R. L. Winslow. Modeling gain and gradedness of Ca^{2+} release in the functional unit of the cardiac diadic space. *Biophys. J.*, 77:1871–1884, 1999.

[52] S. Rush and H. Larsen. A practical algorithm for solving dynamic membrane equations. *IEEE Trans. Biomed. Eng.*, 25:389–392, 1978.

[53] T. R. Shannon, K. S. Ginsburg, and D. M. Bers. Potentiation of fractional sarcoplasmic reticulum calcium release by total and free intra-sarcoplasmic reticulum calcium concentration. *Biophys. J.*, 78(1):334–343, 2000.

[54] T. R. Shannon, F. Wang, J. Puglisi, C. Weber, and D. M. Bers. A mathematical treatment of integrated Ca dynamics within the ventricular myocyte. *Biophys. J.*, 87(5):3351–3371, 2004.

[55] Y. Shiferaw, M. A. Watanabe, A. Garfinkel, J. N. Weiss, and A. Karma. Model of intracellular calcium cycling in ventricular myocytes. *Biophys. J.*, 85:3666–3686, 2003.

[56] W. Shimizu and C. Antzelevitch. Cellular and ionic basis for T-wave alternans under long-QT conditions. *Circulation*, 99:1499–1507, 1999.

[57] M. D. Stern, L. S. Song, H. Cheng, J. S. Sham, H. T. Yang, K. R. Boheler, and E. Rios. Local control models of cardiac excitation-contraction coupling. A possible role for allosteric interactions between ryanodine receptors. *J. Gen. Physiol.*, 113(3):469–489, 1999.

[58] H. Sun, N. Leblanc, and S. Nattel. Mechanisms of inactivation of L-type calcium channels in human atrial myocytes. *Am. J. Physiol. Heart Circ. Physiol.*, 272:H1625–H1635, 1997.

[59] P. Taggart, P. Sutton, Z. Chalabi, M. R. Boyett, R. Simon, D. Elliott, and J. S. Gill. Effect of Adrenergic Stimulation on Action Potential Duration Restitution in Humans. *Circ. Res.*, 33:54–62, 1973.

[60] P. Taggart, P. M. I. Sutton, T. Opthof, R. Coronel, R. Trimlett, W. Pugsley, and P. Kallis.

Inhomogeneous transmural conduction during early ischemia in patients with coronary artery disease. *J. Mol. Cell. Cardiol.*, 32:621–639, 2000.

[61] K. H. W. J. Ten Tusscher, D. Noble, P. J. Noble, and A. V. Panfilov. A model for human ventricular tissue. *Am. J. Physiol. Heart Circ. Physiol.*, 286:H1573–H1589, 2004.

[62] K. H. W. J. Ten Tusscher and A. V. Panfilov. Influence of nonexcitable cells on spiral breakup in two-dimensional and three-dimensional excitable media. *Phys. Rev. E*, 68:062902–1–062902–4, 2003.

[63] K. H. W. J. Ten Tusscher and A. V. Panfilov. Wave propagation in excitable media with randomly distributed obstacles. *Multiscale Model. Simul*, 3:265–282, 2005.

[64] E. G. Tolkacheva, D. G. Schaeffer, D. J. Gauthier, and W. Krassowska. Condition for alternans and stability of the 1:1 response pattern in a "memory" model of paced cardiac dynamics. *Phys. Rev. E. Stat. Nonlin. Soft. Matter. Phys.*, 67(3):031904, 2003.

[65] M. A. Watanabe, F. H. Fenton, S. J. Evans, H. M. Hastings, and A. Karma. Mechanisms for Discordant Alternans. *J. Cardiovasc. Electrophysiol.*, 12:196–206, 2001.

[66] T. Wu, S. Lin, J. N. Weiss, C. Ting, and P. Chen. Two Types of Ventricular Fibrillation in Isolated Rabbit Hearts. *Circulation*, 106:1859–1866, 2002.

[67] A. M. Yue, M. R. Franz, P. R. Robers, and J. M. Morgan. Global endocardial electrical restitution in human right and left ventricles determined by noncontact mapping. *Am. J. Cardiol.*, 46:1067–1075, 2005.

7 Figure Legends

Figure 1

Calcium compartments involved in excitation contraction coupling. L-type calcium channels (I_{CaL}) release calcium in the diadic space or subspace (SS), where sarcolemmal membrane and membrane of the sarcoplasmic reticulum are in close proximity. Ryanodine receptors (J_{rel}) sense this elevation of calcium in the subspace and respond with a release of calcium from the sarcoplasmic reticulum (SR). Through diffusion (J_{xfer}) the calcium released in the subspace travels to the cytoplasm (cyto). Sodium-calcium exchangers (I_{NaCa}) and the sarcolemmal calcium pump (I_{pCa}) pump calcium out of the cytoplasm to the exterior of the cell. Calcium pumps in the membrane of the SR (J_{up}) pump calcium out of the cytoplasm back into the SR. A small leakage current (J_{leak}) leaks calcium from the SR to the cytoplasm.

Figure 2

A Steady-state epicardial action potential shape at 1Hz pacing. **B** Steady-state cytoplasmic calcium transient at 1Hz pacing. **C** Steady-state subspace calcium transient at 1Hz pacing.

Figure 3

A Steady-state subspace calcium inactivation curve. **B** Time constant curve of subspace calcium inactivation. **C** Steady-state curves of slow (f_∞) and fast ($f_{2\infty}$) voltage inactivation. **D** Time constant curves of slow (τ_f) and fast (τ_{f2}) voltage inactivation. Experimental time constants are added for comparison and are taken from Beuckelmann et al., Benitah et al., Mewes et al., Sun et al., Li et al., Pelzmann et al., and Magyar et al. [4, 3, 36, 58, 32, 46, 35].

Inactivation time constant represent the slowest timescale of calcium current inactivation, thus corresponding to f gate inactivation. For recovery from inactivation both fast and slow time constants are available, corresponding to f_2 and f gate recovery. **E** Peak current voltage relationship of the L-type calcium current as determined in simulated voltage clamp experiments. Experimental data are from Magyar et al. [34].

Figure 4

A Schematic drawing of the four-state Ryanodine receptor Markov model of Shannon et al. [54] and Stern et al. [57]. O: open conducting state, R: resting closed state, I: inactivated closed state, RI: resting inactivated closed state. k3 and k4 are constants, the values of k1 and k2 are dependent on SR calcium concentration: opening rate is sped up and closing rate slowed down by higher SR calcium load. In addition, k1 is multiplied by the square of the subspace calcium concentration and k2 is multiplied by the subspace calcium concentration to give a final rate constant: opening and closing rate increase with triggering subspace calcium levels, but opening more so than closing.

B Non-linear gain function of CICR as a function of free calcium concentration in the sarcoplasmic reticulum. Experimental data from Shannon et al. [53] for rabbit ventricular myocytes are added for comparison.

Figure 5

Single cell APD restitution. **A, B, C, D** Restitution curves obtained using a S1S2 restitution protocol for a BCL of 600ms measuring APD at 50% and 90% repolarization for four different

parameter settings of our model (Table 2). Action potential duration is plotted against diastolic interval. Experimental ARI restitution curves are from Nash et al. **E, F, G, H** Restitution curves obtained using a dynamic restitution protocol measuring APD at 90% repolarization for the four same parameter settings. Action potential duration is plotted against diastolic interval. Grey shading is used to indicate the region of the restitution curve where the slope exceeds one. **I, J, K, L** Same dynamic restitution curves as in **E**, **F**, **G** and **H** but now plotting action potential duration against stimulation period. Splitting of the restitution curve indicates the presence of two APDs for a single period: APD alternans.

Figure 6

APD Restitution in a ring for the 12 different model settings. Restitution curves are obtained by initiating a pulse propagating in one direction which propagates until steady state APD is reached after which the ring length and hence BCL is shortened. **A** Restitution for the model setting with a maximum slope of 0.7/0.8 combined with the standard, intermediate and LR fast sodium current dynamics. **B** Restitution for the model setting with a maximum slope of 1.1 combined with the standard, intermediate and LR fast sodium current dynamics. **C** Restitution for the model setting with a maximum slope of 1.4 combined with the standard, intermediate and LR fast sodium current dynamics. **D** Restitution for the model setting with a maximum slope of 1.8/1.9 combined with the standard, intermediate and LR fast sodium current dynamics.

Figure 7

Snapshots of spiral wave dynamics for the 12 different model settings. Columns: **Column 1** standard sodium dynamics, **Column 2** intermediate sodium current dynamics, **Column 3** LR sodium current dynamics. Rows: **Row 1** slope 0.7/0.8 setting, **Row 2** slope 1.1 setting, **Row 3** slope 1.4 setting, **Row4** slope 1.8/1.9 setting. If spiral breakup occurs, the time of first wave break is indicated in the upper left corner.

Figure 8

A Conduction velocity restitution for the shallow parameter setting of our model (slope 0.8) combined with the standard, intermediate and LR fast sodium current dynamics. Restitution was measured in a cable of 800 cells. **B** Period (three upper lines) and diastolic interval (three lower lines) as a function of time, for spiral wave rotation for the shallow parameter setting of our model combined with the standard, intermediate and LR fast sodium current dynamics

Figure 9

Snapshots of spiral wave dynamics for 4 different model settings. **A** Slope 1.1, standard sodium current dynamics $G_{Na} \times 7$ **B** Slope 1.1, LR sodium current dynamics $G_{Na} \times 0.4$ **C** Slope 1.4, standard sodium current dynamics $G_{Na} \times 7$ **D** Slope 1.4, LR sodium current dynamics $G_{Na} \times 0.4$

8 Figures

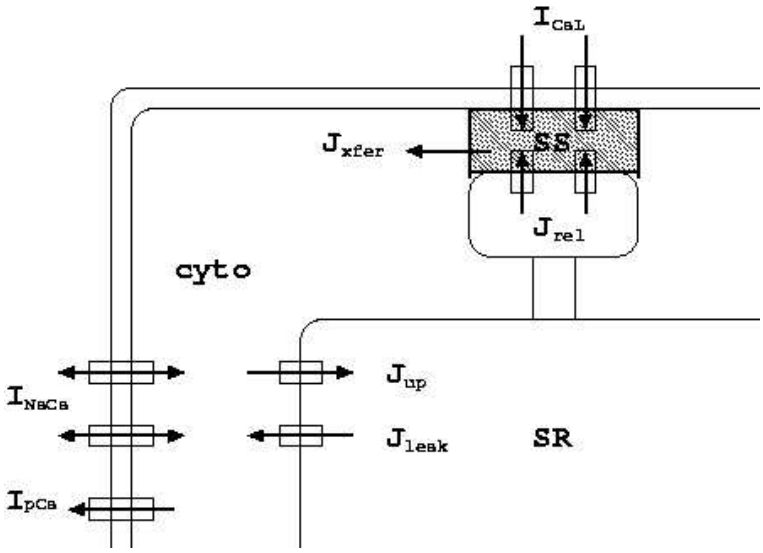

Figure 1:

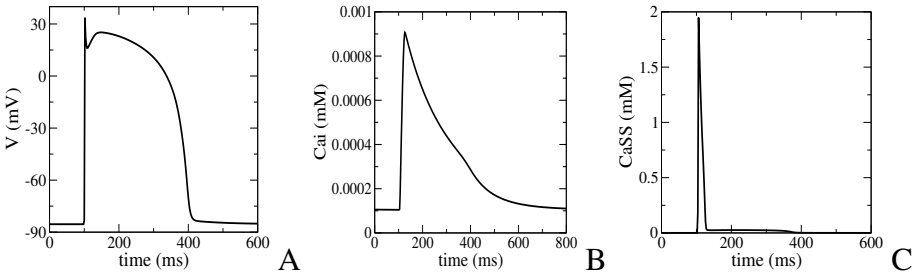
30
0
-30
-60
-90
V (mV)
0
200
400
600
time (ms)
A
0.001
0.0008
0.0006
0.0004
0.0002
0
Cai (mM)
0
200
400
600
800
time (ms)
B
2
1.5
1
0.5
0
CaSS (mM)
0
200
400
600
time (ms)
C

Figure 2:

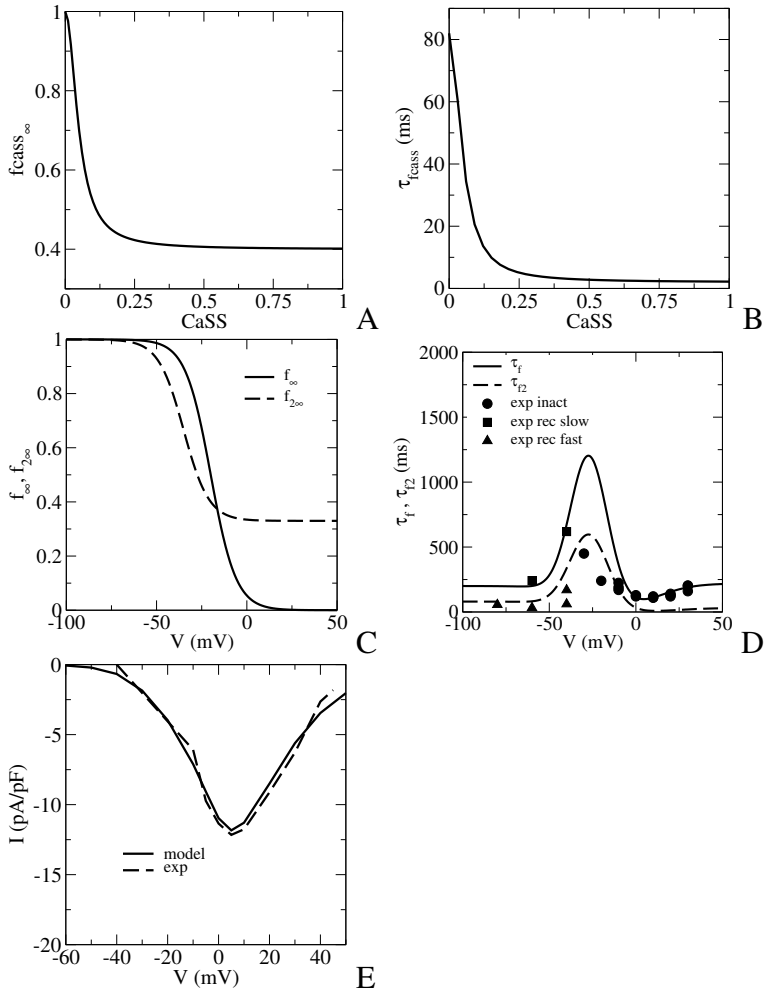
fcass∞
CaSS
A
τfcass (ms)
CaSS
B
f∞, f2∞
f∞
f2∞
V (mV)
C
τf, τf2 (ms)
τf
τf2
exp inact
exp rec slow
exp rec fast
V (mV)
D
I (pA/pF)
model
exp
V (mV)
E

Figure 3:

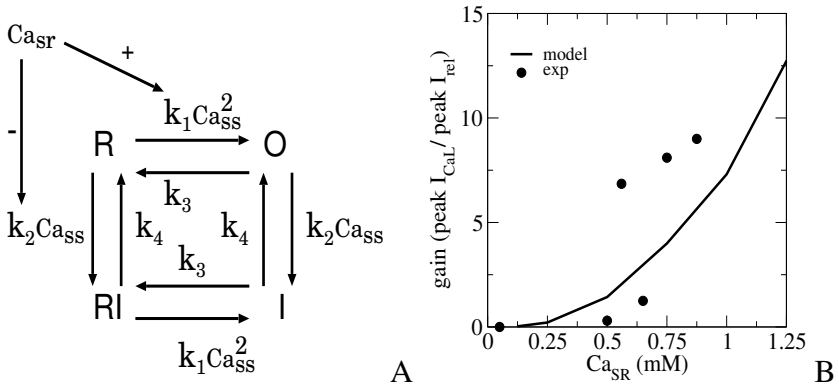
Ca_sr
+
-
k1Ca2ss
R
O
k3
k2Cass
k4
k4
k2Cass
k3
RI
I
k1Ca2ss
A
model
exp
gain (peak ICaL / peak Irel)
15
10
5
0
0
0.25
0.5
0.75
1
1.25
CaSR (mM)
B

Figure 4:

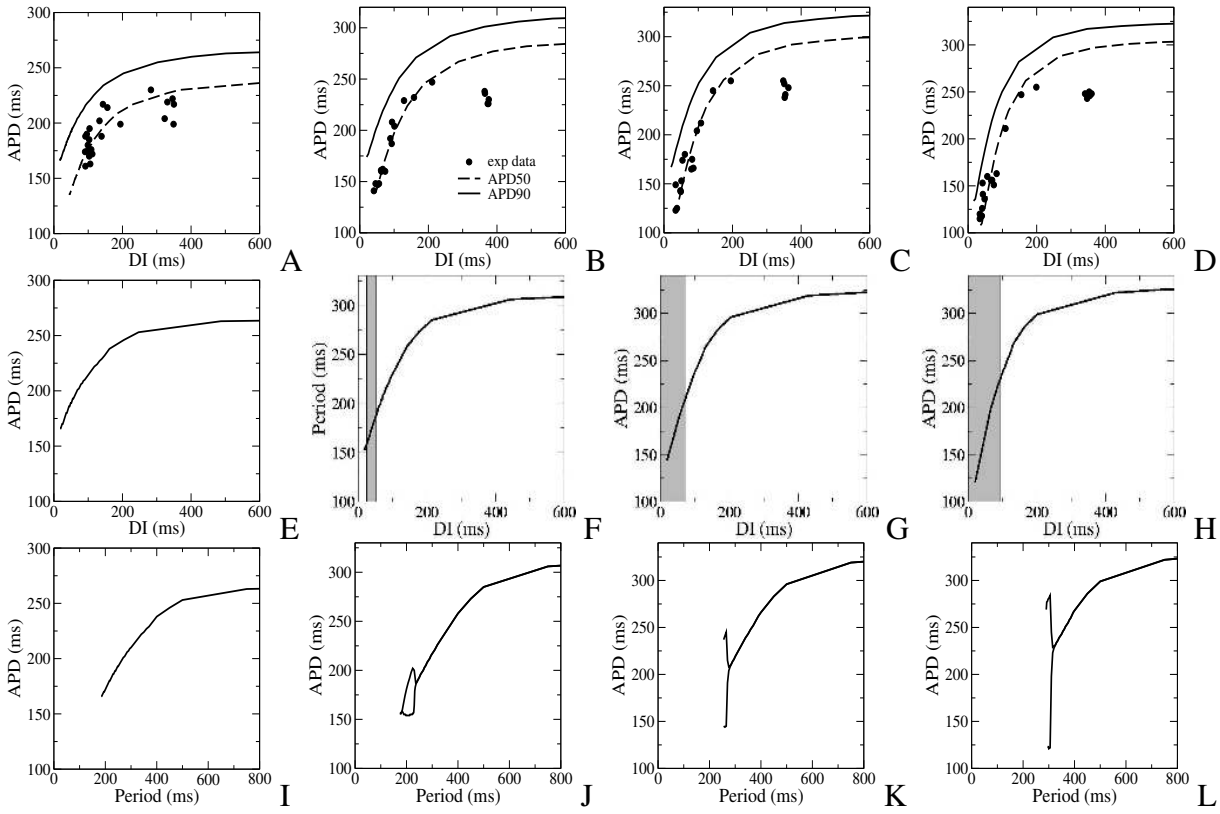

Figure 5:

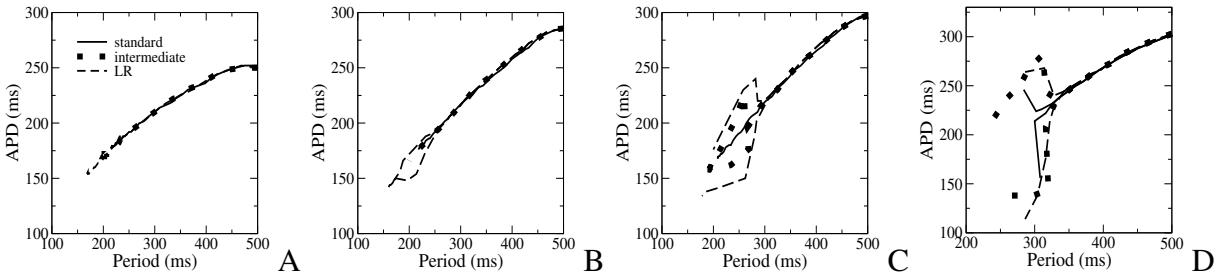

Figure 6:

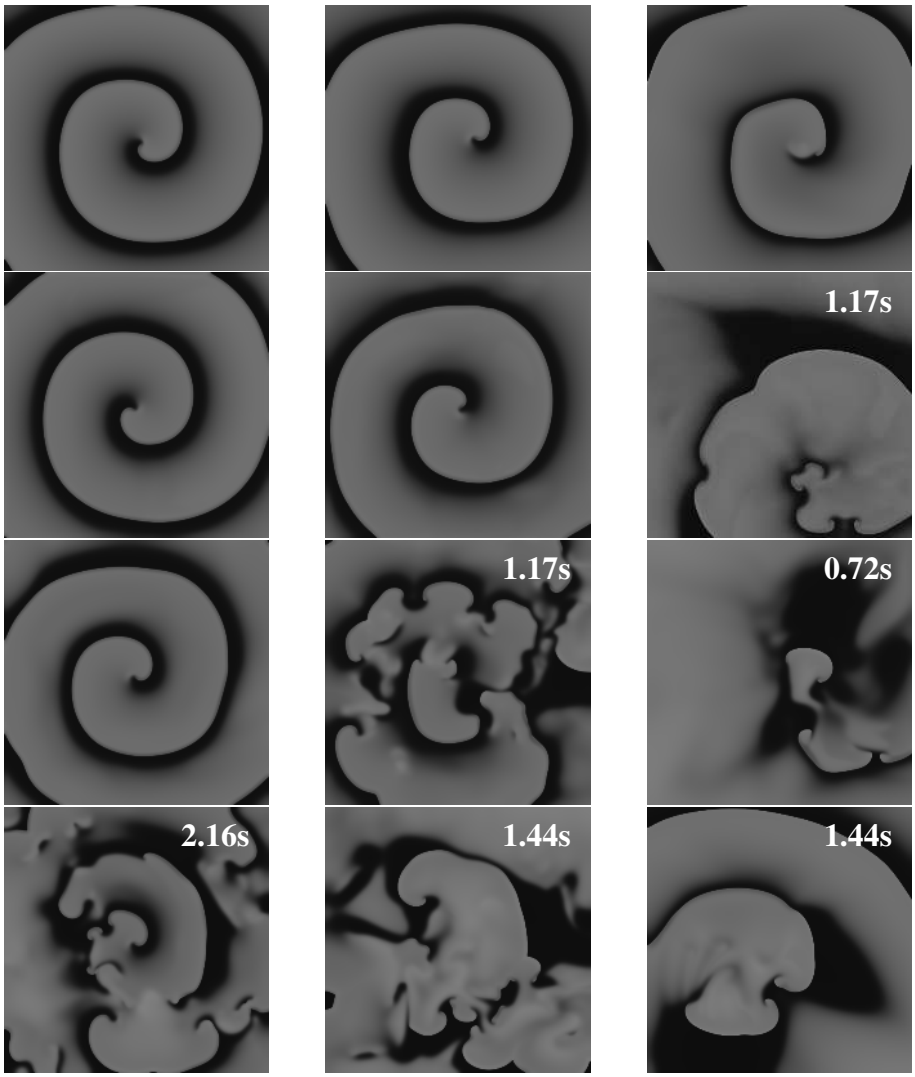

Figure 7:

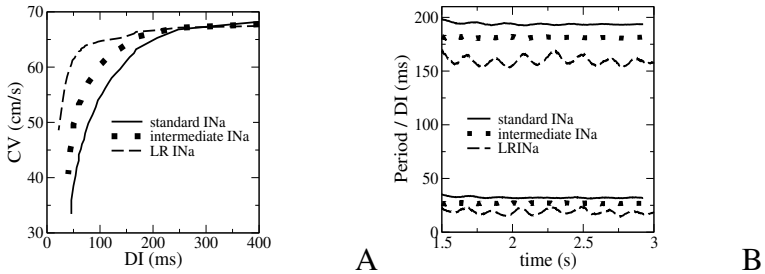
CV (cm/s)
DI (ms)
standard INa
intermediate INa
LR INa
Period / DI (ms)
time (s)
standard INa
intermediate INa
LRINa

A B

Figure 8:

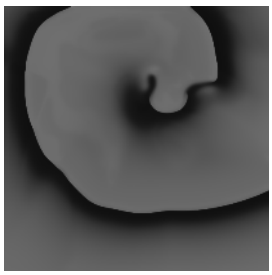
A
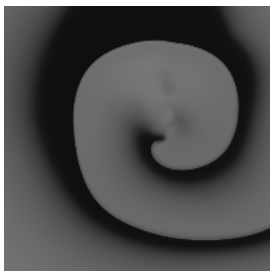
B
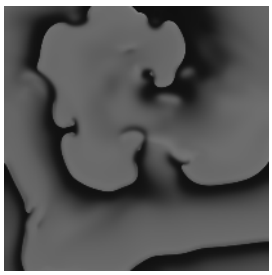
C

D

Figure 9:

9 Tables

Table 1 Default model parameter settings.

Parameter	Definition	Value
R	Gas constant	$8.3143 JK^{-1}mol^{-1}$
T	Temperature	$310K$
F	Faraday constant	$96.4867 Cmmol^{-1}$
C_m	cell capacitance per unit surface area	$2.\mu F cm^{-2}$
S	surface to volume ratio	$0.2\mu m^{-1}$
ρ	cellular resistivity	$162\Omega cm$
V_c	cytoplasmic volume	$16.404\mu m^3$
V_{sr}	sarcoplasmic reticulum volume	$1.094\mu m^3$
V_{ss}	subspace volume	$0.05468\mu m^3$
K_o	Extracellular K^+ concentration	$5.4mM$
Na_o	Extracellular Na^+ concentration	$140mM$
Ca_o	Extracellular Ca^{2+} concentration	$2mM$
G_{Na}	Maximal I_{Na} conductance	$14.838 nSpF^{-1}$
G_{K1}	Maximal I_{K1} conductance	$5.405 nSpF^{-1}$
G_{to}, epi, M	epicardial I_{to} conductance	$0.294 nSpF^{-1}$
G_{to}, endo	Maximal endocardial I_{to} conductance	$0.073 nSpF^{-1}$

Continued on next page

Continued from previous page

Parameter	Definition	Value
G_{Kr}	Maximal I_{Kr} conductance	$0.153 nS pF^{-1}$
G_{Ks}, epi, endo	Maximal epi and endocardial I_{Ks} conductance	$0.392 nS pF^{-1}$
G_{Ks}, M	Maximal M cell I_{Ks} conductance	$0.098 nS pF^{-1}$
p_{KNa}	Relative I_{Ks} permeability to Na^{+}	0.03
G_{CaL}	Maximal I_{CaL}conductance	$3.980^{-5} cm ms^{-1} \mu F^{-1}$
k_{NaCa}	Maximal I_{NaCa}	$1000 pA pF^{-1}$
γ	Voltage dependence parameter of I_{NaCa}	0.35
K_{mCa}	Ca_i half saturation constant for I_{NaCa}	$1.38 mM$
K_{mNai}	Na_i half saturation constant for I_{NaCa}	$87.5 mM$
k_{sat}	Saturation factor for I_{NaCa}	0.1
α	Factor enhancing outward nature of I_{NaCa}	2.5
P_{NaK}	Maximal I_{NaK}	$2.724 pA pF^{-1}$
K_{mK}	K_o half saturation constant of I_{NaK}	$1 mM$
K_{mNa}	Na_i half saturation constant of I_{NaK}	$40 mM$
G_{pK}	Maximal I_{pK} conductance	$0.0146 nS pF^{-1}$
G_{pCa}	Maximal I_{pCa} conductance	$0.1238 nS pF^{-1}$
K_{pCa}	Half saturation constant of I_{pCa}	$0.0005 mM$
G_{bNa}	Maximal I_{bNa} conductance	$0.000290 nS pF^{-1}$

Continued on next page

Continued from previous page

Parameter	Definition	Value
G_{bCa}	Maximal I_{bCa} conductance	$0.000592 nSpF^{-1}$
V_{maxup}	Maximal I_{up} conductance	$0.006375 mMms^{-1}$
K_{up}	Half saturation constant of I_{up}	$0.00025 mM$
V_{rel}	Maximal I_{rel} conducatance	$40.8 mMms^{-1}$
k_1'	R to O and RI to I I_{rel} transition rate	$0.15 mM^{-2}ms^{-1}$
k_2'	O to I and R to RI I_{rel} transition rate	$0.045 mM^{-1}ms^{-1}$
k_3	O to R and I to RI I_{rel} transition rate	$0.060 ms^{-1}$
k_4	I to O and RI to I I_{rel} transition rate	$0.000015 ms^{-1}$
EC	Ca_{SR} half saturation constant of k_{casr}	$1.5 mM$
max_{sr}	maximum value of k_{casr}	$2.5(dimensionless)$
min_{sr}	minimum value of k_{casr}	$1(dimensionless)$
V_{leak}	Maximal I_{leak} conductance	$0.00036 mMms^{-1}$
V_{xfer}	Maximal I_{xfer} conductance	$0.0038 mMms^{-1}$
Buf_c	Total cytoplasmic buffer concentration	$0.2 mM$
K_{bufc}	Ca_i half saturation constant for cytoplasmic buffer	$0.001 mM$
Buf_{sr}	Total sarcoplasmic buffer concentration	$10 mM$
K_{bufsr}	Ca_{SR} half saturation constant for sarcoplasmic buffer	$0.3 mM$
Buf_{ss}	Total subspace buffer concentration	$0.4 mM$

Continued on next page

Continued from previous page

Parameter	Definition	Value
K_{bufss}	Ca_{SS} half saturation constant for subspace buffer	$0.00025mM$

Table 2 Four different model parameter settings. Parameter values for the setting with a restitution slope of 1.1 correspond to the values in Table 1. Parameters that were varied were maximum conductance of the I_{Kr}, I_{Ks}, I_{pCa} and I_{pK} currents (all in nS/pF). An additional parameter that was used was the time constant for the f gate. For the slope 1.1 setting the time constant was as given in Fig. 3D, for the other settings the time constant was multiplied by a factor (given in the Table) for the voltage range $V > 0mV$, thus rescaling inactivation but not recovery kinetics.

par. setting	G_{Kr}	G_{Ks}	G_{pCa}	G_{pK}	τ_f inact
slope 0.7	0.134	0.270	0.0619	0.0730	$\times 0.6$
slope 1.1	0.153	0.392	0.1238	0.0146	normal
slope 1.4	0.172	0.441	0.3714	0.0073	$\times 1.5$
slope 1.8	0.172	0.441	0.8666	0.00219	$\times 2$

Table 3 Dependence of spiral wave period and diastolic interval on I_{Na} recovery dynamics and size. Spiral wave simulations were performed for the parameter settings with a slope 0.7/0.8 to ensure stable spiral wave rotation for all I_{Na} dynamics. I_{Na} dynamics are either the standard dynamics of our human ventricular cell model or the LR dynamics. I_{Na} conductance is either as for the default parameter settings of our model (Table 1) or multiplied by the indicated factor. Period and DI are mean values and are in ms.

I_{Na} dyn	G_{Na}	Period	DI
standard	normal	194	32
LR	normal	168	19
standard	$\times 7$	184	22
LR	$\times 0.4$	196	29